An Aeroacoustic Investigation of a Tiltwing eVTOL Concept Aircraft*

Ross J. Higgins† and George N. Barakos‡
University of Glasgow, James Watt South Building, Glasgow, G12 8QQ, U.K.

Shahrokh Shahpar§ and Indi Tristanto¶
Rolls-Royce plc., Derby, DE24 8BJ, U.K.

With the advancement in electric battery design, aircraft designers and manufacturers are no longer constrained to established configurations. Developments in Vertical Take-off and Landing (VTOL) aircraft have also been seen in recent times through the design of modern tiltrotor aircraft such as the AW609 and the V-280 Valor. The combination of these developments allowed engineers to propose designs which utilise the vertical take-off and landing capabilities of a tiltrotor aircraft with electrically driven propulsion systems, deemed eVTOL (Electrically driven Vertical Take-off and Landing). This investigation aims to develop an understanding of the aeroacoustic emissions associated with an eVTOL aircraft, due to acoustics being one of the key components in future certification. The study will consist of an investigation into the baseline design, followed by an optimisation study aiming to reduce the amount of noise generated.

Nomenclature

Latin

c	=	Reference Chord (m)
C_p	=	Surface pressure coefficient
C_T	=	Thrust coefficient
D	=	Blade diameter (m)
k	=	Turbulence kinetic energy (m^2/s^2)
S	=	Wing Span (m)
R	=	Blade radius (m)
R/c	=	Blade aspect ratio

†Research Assistant, CFD Laboratory.
‡Professor, CFD Laboratory, corresponding author.
§RR Engineering Fellow, Aerothermal Design System, Innovation Hub, Future Methods
¶Innovation Hub, Future Methods

T = Dimensional time (s)

T^* = Non-dimensional time (-)

V_{ref} = Reference Velocity (m/s)

V_{tip} = Tip velocity (m/s)

V_∞ = Freestream velocity (m/s)

Greek

κ = Reduced Frequency (-)

ρ = Density (kg/m^3)

ω = Specific rate of dissipation (1/s)

Acronyms

CFD = Computational Fluid Dynamics

CFL = Courant-Fridrichs-Lewy condition

eVTOL = Electrical Vertical Take-off and Landing

HMB3 = Helicopter Multi-Block 3

IMPACTA = Improving the Propulsion Aerodynamic and aCoustics of Turboprop Aircraft

JORP = Joint Open Rotor Propeller

MUSCL = Monotone Upstream-centred Schemes for Conservation Laws

OSPL = Overall Sound Pressure Level

UofG = University of Glasgow

URANS = Unsteady Reynolds-Averaged Navier-Stokes

Introduction

With the advancement in the design of electric batteries [1], designers and manufacturers are no longer constrained to standard aircraft designs. These designs no longer have to include the fuel based propulsion systems of typical aircraft as they now have the potential to be replaced with environmentally friendly electric systems. Developments in Vertical Take-off and Landing (VTOL) aircraft have also been seen in recent times through the design of modern tiltrotor aircraft such as the AW609 and the V-280 Valor.

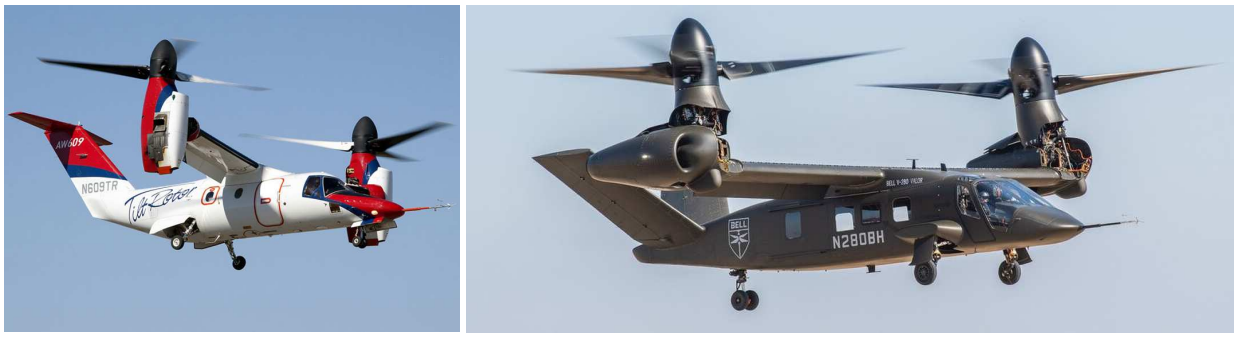

(a) AW609 (b) V-280

Fig. 1 Recent tiltrotor aircraft designs

The combination of these developments has allowed engineers to develop designs which utilise the vertical take-off and landing capabilities of a tiltrotor aircraft with electrically driven propulsion systems, deemed eVTOL (Electrically driven Vertical Take-off and Landing) [2].

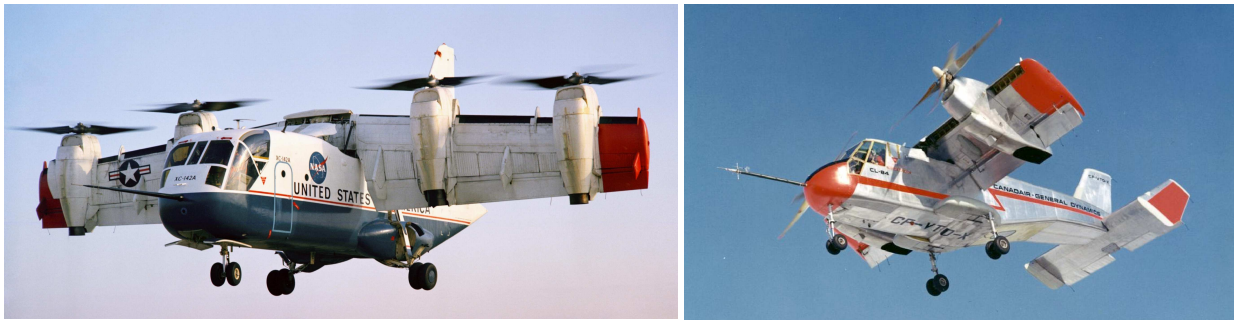

(a) XC-142 (b) CL-84

Fig. 2 Tiltwing configurations developed in the 1960s

The possibility of an electric propulsion system has also made it possible to revisit the tiltwing concept that was demonstrated in the XC-142 and CL-84. Cross-shafting can be achieved by simpler electrical connection between motors. This combination is seen as a key enabler in a new dimension of aerospace research which focuses on light flying machines suitable for air-taxi operations which work in conjunction with current urban transport systems. Such a concept has been developed by Rolls-Royce and will be used for this investigation.

One of the key challenges associated with an electrically driven multi-rotor aircraft design is its aeroacoustic

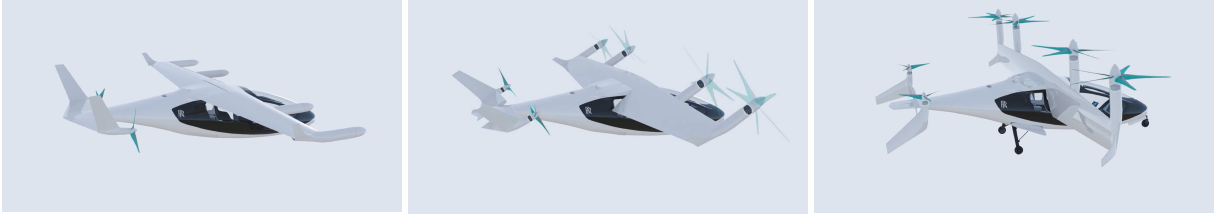

Fig. 3 Rolls-Royce eVTOL tiltwing concept aircraft

emissions. New European regulations are to be introduced in 2020 which aims to reduced the acoustic footprint of aircraft by 50% [3], with a total noise abatement of 65% by 2050 [4]. As a result of this, an investigation is required which aims to understand and reduce the amount of noise generated by the eVTOL concept aircraft. For this investigation, high fidelity Computational Fluid Dynamics (CFD) will be used.

HMB3

For this investigation, the in-house CFD solver Helicopter-Multi-Block-3 (HMB3) is used. The core functionality of HMB3 is CFD, however, its use has been extended in recent years to include whole engineering applications, including helicopter rotor aeroelasticity [5], propeller aeroacoustics [6], flight mechanics [7] and missile trajectory prediction [8]. Previous investigations using HMB3 have provided propeller flow validation in both installed and isolated conditions, by comparison with the experimental results of the Joint Open Rotor Propeller (JORP) blade [9], the Improving the Propulsion Aerodynamic and aCoustics of Turboprop Aircraft (IMPACTA) wind tunnel tests [10, 11] and the model aircraft propeller inflow investigation at the University of Glasgow. Good agreement in terms of aerodynamics, acoustics and aeroelasticity were seen by all [12–15]. In addition to propeller flows, HMB3 has also been validated for tiltrotors, including the AW609 and XV-15 [16], for hover and forward flight. Further validation was conducted on a model scale propeller which was experimentally studied by Rolls-Royce.

Mesh Structure

Multi-block structured meshes are used with HMB3, which allow an easy sharing of the calculation load for parallel simulations. ICEM-Hexa™ of ANSYS is used to generate the mesh. An overset grid method is available in HMB3 [17], to allow for relative motions between mesh components. The chimera method is based on composite grids, consisting of independently generated, overlapping non-matching sub-domains, hence simplifying the mesh generation. Each of these sub-domains are referred to as a Levels and are sorted hierarchically, with higher levels having priority. The exchange of information between sub-domains is achieved through interpolation and by following the hierarchy of mesh levels [17].

Turbulence Modelling

Various turbulence models are available in the HMB3 solver, which includes several one-equation, two-equation, and four-equation turbulence transition models. Furthermore, Large-Eddy Simulation (LES), Detached-Eddy Simulation (DES) [18], Delay-Detached-Eddy Simulation (DDES) [19], and Scale-Adaptive Simulation (SAS) [20, 21] options are also available. In this work, the $k-\omega$ turbulence model was used to close the URANS equations due to the fact that tonal noise is the main component for this aircraft.

eVTOL Aircraft Simulation

The key focus of this investigation involves the simulation of the full Rolls-Royce aircraft for acoustic emissions using the HMB3 CFD solver. Focus initially placed on the the simulation of the aircraft during hover flight, with a transition to forward flight following the completion of the hover simulations.

Grid Generation

The chimera grid method is used for the full aircraft. This allows the individual components of the aircraft to the meshed within it's own sub-domain. A total of five chimera levels are used and these include the blades, main/tail wing and fuselage. An additional circular drum level between the blades and main/tail wings is introduced to improve the interpolation. Figure 4 presents the hierarchy of solid wall components.

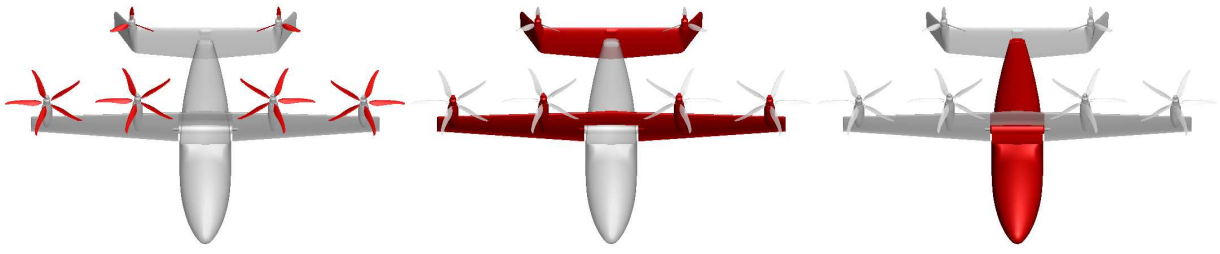

(a) Propeller blades (Level 5) (b) Main and tail wing (Level 3) (c) Fuselage (Level 2)

Fig. 4 Aircraft solid wall components (with chimera levels shown)

Fully Assembled Grids

Table 1 details the grid size and chimera level for each sub-domain for the semi-span aircraft simulations in hover and forward flight. The largest individual sub-domain is the fuselage grid in both hover and forward-flight. This is to ensure enough cells are present around both the tail and wing to ensure sufficient interpolation. In forward-flight the front propeller blades are folded, hence these grids and the front drum are not required for this test condition. A spacing of $1 \times 10^{-6} c_{ref}$ is applied to the cells normal to all solid surfaces. This ensures a $Y+$ value less than 1.0.

Grid Component	Hover		Forward-Flight	
	Grid Size	Level	Grid Size	Level
Background	12,250,000	1	12,250,000	1
Fuselage	26,654,587	2	28,663,627	2
Wing	20,853,912	3	17,441,402	3
Tail	13,077,920	3	12,712,160	3
Front Drum	9,313,504	4	*n/a*	-
Rear Drum	3,672,000	4	3,672,000	4
Front Propellers	3,911,100 *x2*	5	*n/a*	-
Rear Propellers	5,023,188	5	5,023,188	5
Total	98,667,311	-	79,762,377	-

Table 1 Grid summary for the semi-span aircraft in hover and forward-flight

Presented in Figure 5 is the visualisation of the computational domain and chimera boundaries for the key components. The size of the domain does not change between hover and forward flight. The topology used for the wing and tail in forward-flight is adjusted to ensure sufficient interpolation between these components and the lower level fuselage grid. The adjustments are focused around the wing/tail-fuselage junctions.

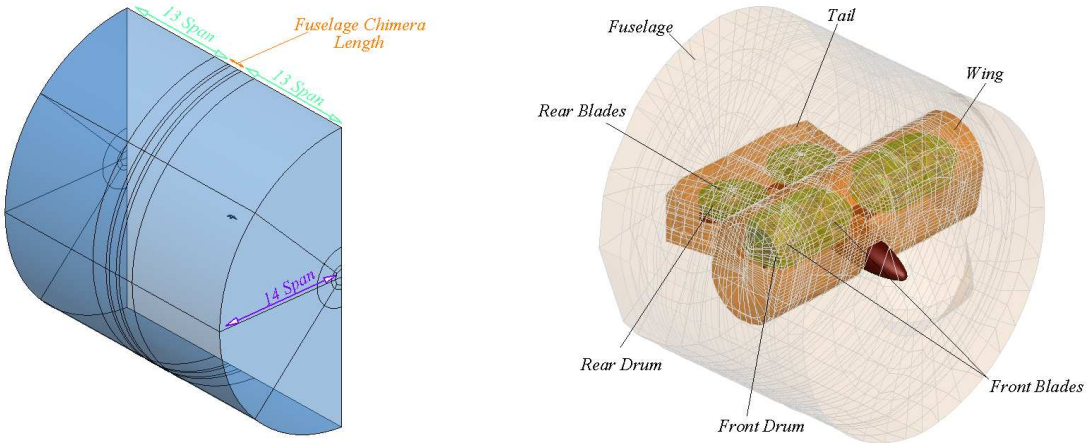

(a) Computational domain

(b) Key grid sub-domains

Fig. 5 eVTOL aircraft chimera grid in hover

Numerical Probes and Grid Pre-Process

Due to the size of the computational grid, the storing of large flow-field solutions can be problematic. Therefore, numerical probes are inserted into the grid to ensure the flow-field solution can be stored at several locations at each time-step. In addition to storing the flow-field variables (pressure, density, velocity and all turbulence variables) for future post-processing, it also enables the monitoring of the solution.

Several probes are used for this simulation across the fuselage, wing and a fictitious ground plane. The ground plane is located 3 span-lengths (S) vertically downstream of the aircraft with a width and length of $5S$ and $7S$, respectively. A total of 1043 probes are used across this plane. Several slices are taken across the main wing and fuselage with 501 and 576 probes, respectively.

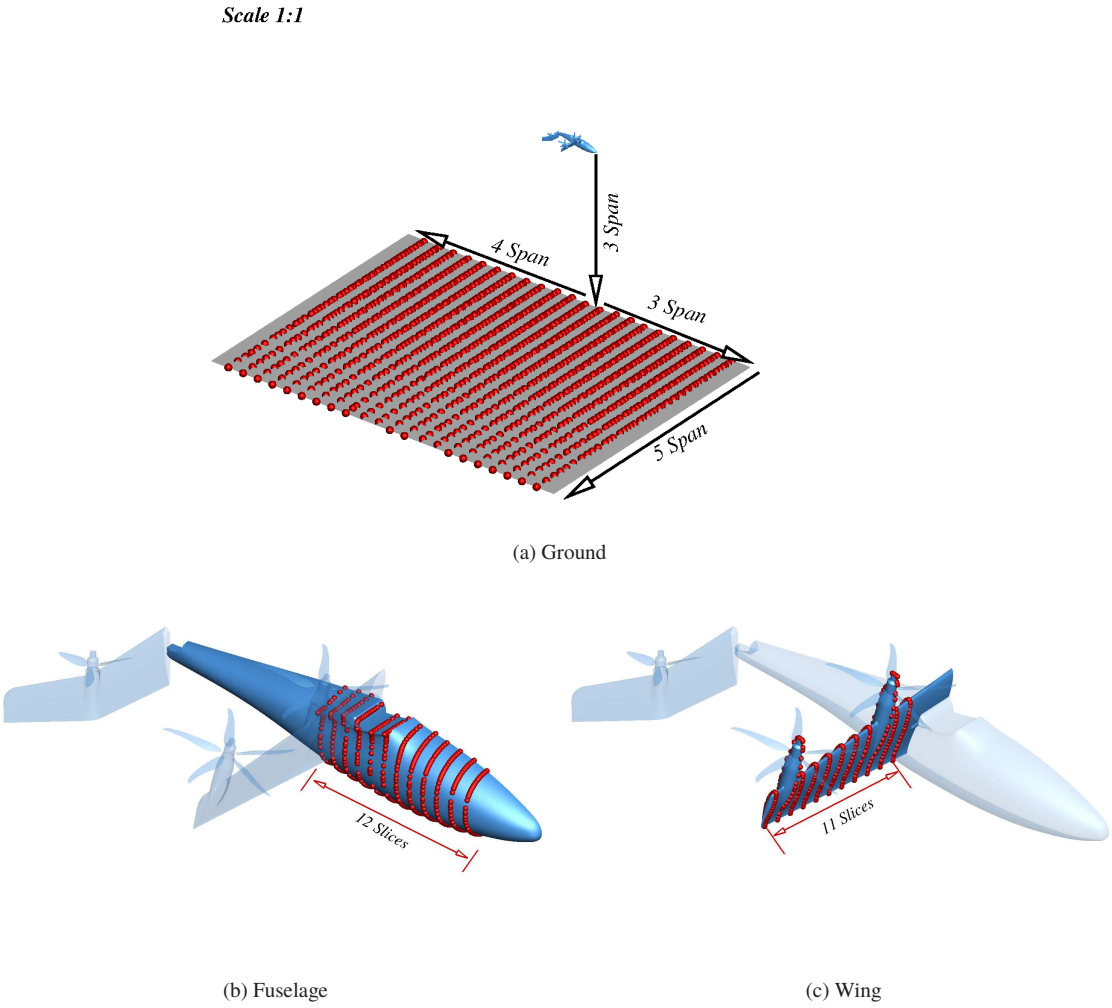

(a) Ground

(b) Fuselage

(c) Wing

Fig. 6 Numerical probes for the monitoring of acoustic emissions

Simulation Setup

With the semi-span grid defined, the following section will detail the test conditions for the simulation of the aircraft in hover and forward-flight using the Unsteady Reynolds-Averaged Navier-Stokes (URANS) equations with the baseline $k-\omega$ turbulence model.

Test Conditions

Presented below in Table 2 is the test conditions simulated using HMB3 in hover. As the simulation will be conducted in hover with zero freestream velocity, the reference velocity for the Mach and Reynolds number is taken as the front blade tip velocity. The front blade root chord is also used as the reference length.

Reference Reynolds Number (-)	$\sim 2 \times 10^6$
Reference Mach Number (-)	~ 0.6
Freestream Velocity (m/s)	0.0
Ambient Conditions	*Sea-level*
Simulation Method	*URANS*
Turbulence Modelling	$k-\omega$

Table 2 Summary of the test conditions for the semi-span aircraft in hover.

Presented below in Table 3 is the test conditions simulated using HMB3 in forward-flight. The reference chord length is kept constant with the reference Mach and Reynolds numbers adjusted to the freestream velocity conditions. The propeller rotational velocity is applied via the rigid body rotation with an updated reduced frequency required based upon the tip and freestream velocities.

Reference Reynolds Number (-)	$\sim 0.4 \times 10^6$
Reference Mach Number (-)	~ 0.12
Ambient Conditions	*Sea-level*
Simulation Method	*URANS*
Turbulence Modelling	$k-\omega$

Table 3 Summary of the test conditions for the semi-span aircraft in forward-flight.

Results of the Semi-Span Aircraft in Hover

Aerodynamics

Presented in Figure 7 is the time-history of the propeller blade normalised C_T. The loads have been normalised with respect to the average outer front propeller thrust value. As observed from the two front propellers, there is a periodic fluctuation in the loads in where the load reduces by 23% and 20% from the average for the inner and outer front propeller, respectively. This reduction correlates to the blade passing the wing, with the largest reduction coming as both propellers cross the mid-section. The average individual blade normalised C_T values are seen to be 0.1967 and 0.2004 for the front inner and outer propellers, respectively. The reduction in blade thrust coefficient is seen to be sharper for the inner propeller than the outer. This is the result of the outer propeller having less blockage downstream.

Oscillations due to the presence of the tail wing are also seen in the rear blade loads, however, these are smaller than the oscillation seen in both front propellers. The average rear blade has a normalised thrust coefficient of 0.1869 with a fluctuation around this average of ±8%. The fluctuation around the average is symmetrical due to the twice per revolution influence of the tail and the centre equivalent span length placement of the propeller.

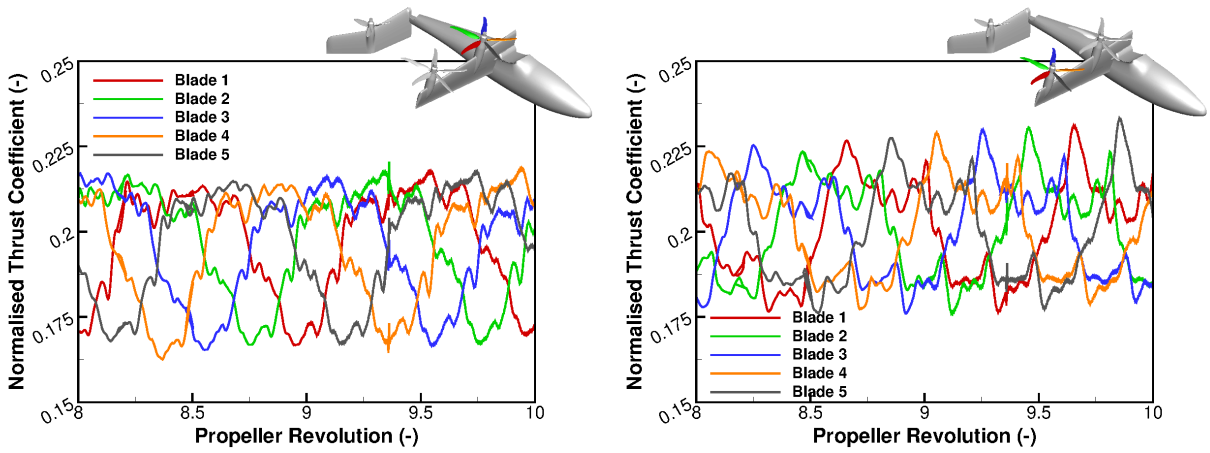

(a) Front inner blades

(b) Front outer blades

(c) Rear blades

(d) Full propeller

Fig. 7 Individual blade and full propeller normalised C_T time history

The combined normalised C_T for each propeller is presented in Figure 7(d). The fluctuations in thrust coefficient for both of the front propellers is observed, however, their percentage with respect to the revolution average has significantly reduced when compared to individual blade loads. Average C_T values of 0.9837, 1.0 and 0.8489 were seen for the front inner, front outer and rear propellers, respectively. The average fluctuations are 2.44%, 1.71% and 4.6% for the front inner, front outer and rear propellers, respectively.

The individual blade loads indicated a significantly higher influence of the wing blockage on the inner propeller due to the sharp reduction in C_T. This influence is also observed in the full propeller loads. A higher C_T value and lower percentage fluctuation is seen for the outer front propeller due to this propeller having less obstruction downstream. The largest percentage fluctuation is seen at the rear propeller. This is due to the vertical placement of the propeller with the rear nacelle distance less than half the front.

Presented in Figure 8 is the normalised surface pressure coefficient across the full vehicle (the solution has been mirrored in Tecplot to prove greater clarity). The surface pressure coefficients were saturated with respect to the front propeller blade tip velocity before scaling by the maximum value seen across the fixed aircraft components. Due to the top-in rotation of each propeller, the negative pressure component is seen towards the centre of the aircraft for each propeller with the positive component on the opposite side of the nacelle on the pressure side of the wing. A similar profile is seen along the tail with positive pressure component seen along the vertical-fin section and a negative along the horizontal. Due to the design of the tail, a band of negative pressure is enclosed between the horizontal and vertical junction.

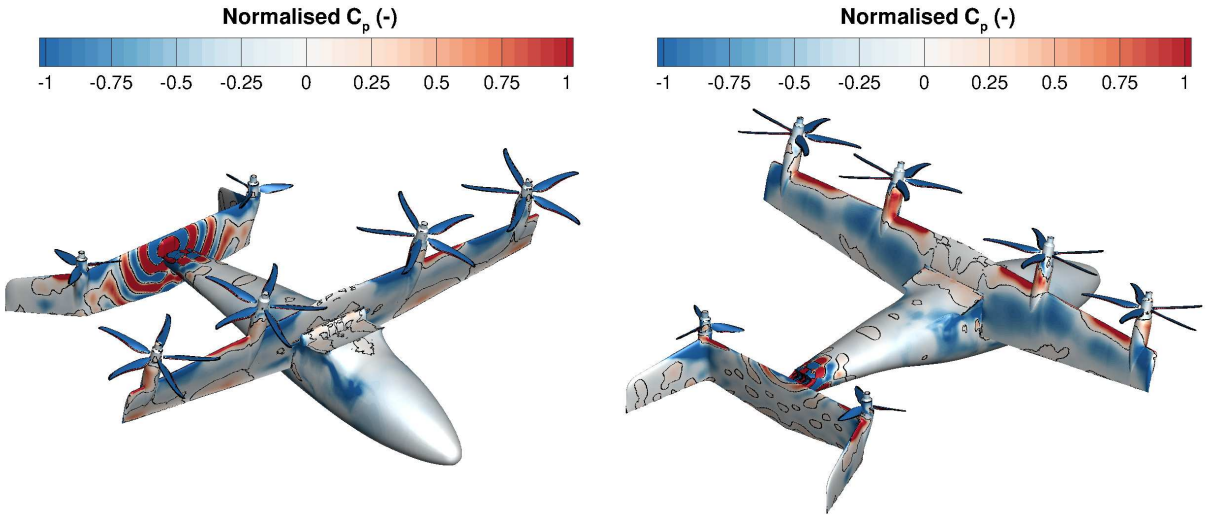

Fig. 8 Aircraft normalised surface pressure coefficient

Acoustics

Presented in Figure 9 is the instantaneous non-dimensionalised Overall Sound Pressure Level (OSPL) for the aircraft in hover. The scale has been non-dimensionalised with respect to the maximum integer ten value seen on the surface. Sound levels above 0.7 are observed across the entire aircraft surface, with values below 0.6 only seen in the troughs of the waves. The main sources of noise are the propellers, where the maximum noise levels are seen towards the tips. Looking at the front propellers, higher noise levels are seen on the outer blades. This is expected based upon the high thrust coefficient seen for the outer propellers. For the rear propellers, values above 0.8 are seen across the entire blades. Although the rear propellers are not lifting as much as the front, the tail section is twice as close to the blades as the wing is to the front, therefore the interaction between the rear propeller and tail has a greater influence.

An additional source of noise is observed at the wing-fuselage pivot junction. This is a secondary result of the front propellers and is the tip vortex impinging on the junction. As the tip vortex periodically impacts the junction, an acoustic wave is generated and pulsates across the fuselage surface. Noise levels at the maximum value are observed at the junction with the pulses dissipating down to 0.8.

A third source, and perhaps the greatest consequence of the propeller blade propulsion, are the fluctuations seen at the tail-fuselage junction. High frequency and high value sound waves are generated around this region and propagate into the flow-field. Values around, and above, the maximum are observed at certain instances. These waves are generated from the reflection of the rear propeller waves and the wing-fuselage pivot junction waves which propagate rearwards towards the tail. As the wing-fuselage waves travel towards the tail, the 90° angle reflects these towards the lower frequency rear propeller emissions resulting in an amplification of both noise and frequency.

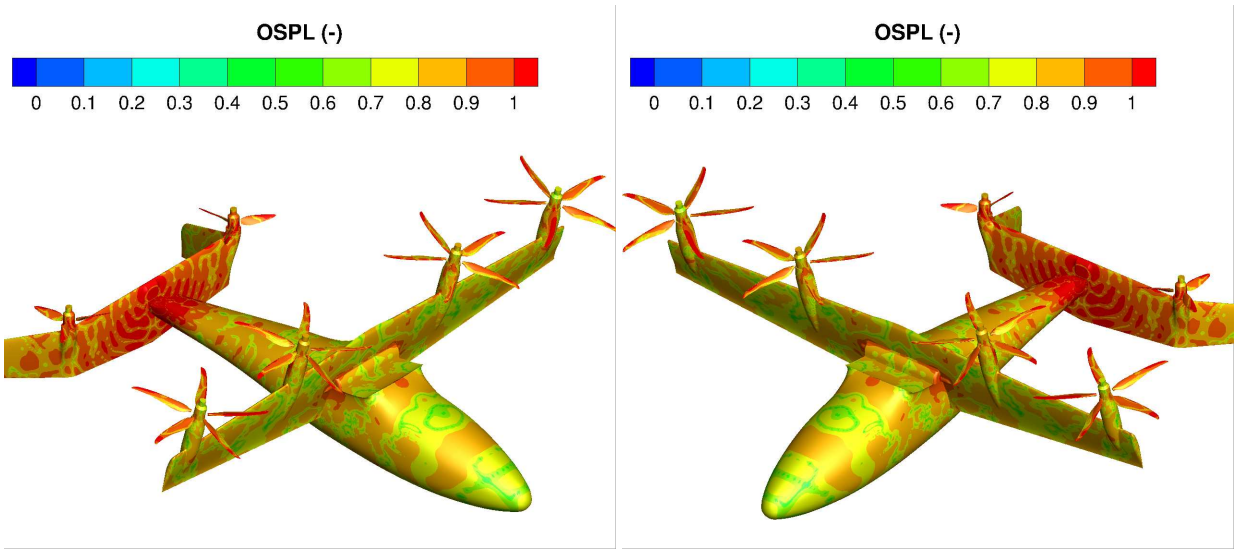

Fig. 9 Instantaneous surface non-dimensional overall sound pressure level (OSPL) for the aircraft in hover

Some of the highest values of OSPL are seen at the front propeller blades. This correlates with the high thrust coefficient produced by each blade, however, it is also influenced by a significant blade vortex interaction. The blade-to-blade interaction is highlighted in Figure 10, where the tip vortex of the blade in-front impinges on the following blade. This occurs over the majority of the revolution, except during the phase in which the blade passes the centre section of the wing. This is also where the blade thrust is at its lowest. The reduction in thrust results in a reduction of the tip vortex strength, thus allowing it to pass under the following blade.

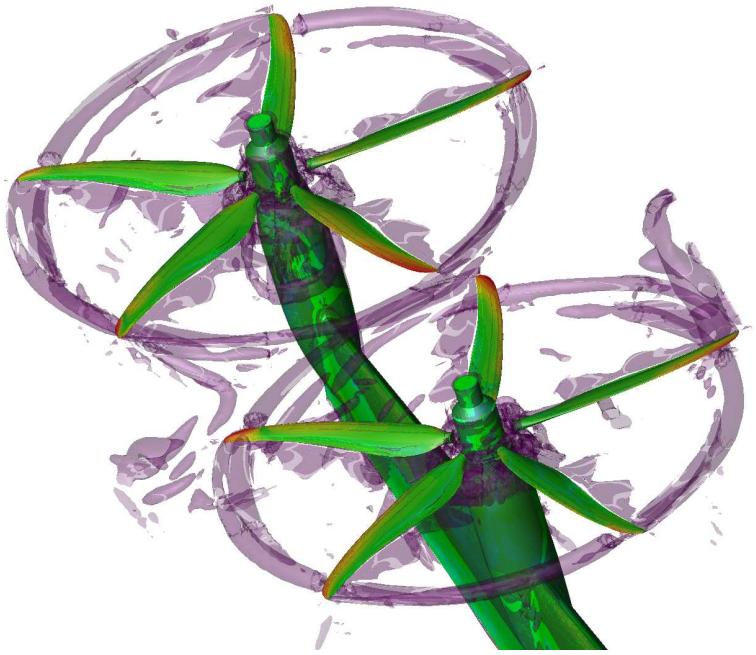

Fig. 10 Front propeller blade vortex interaction

Presented in Figure 11 is the OSPL at selected numerical probes on the fuselage, wing and ground plane. The probes on the fuselage, as expected from the surface OSPL (Figure 9), indicate high values of acoustic noise with fluctuations seen between the maximum value and 0.6. Looking at the probe furthest towards the nose, a clear lower frequency oscillation is observed with a wavelength of approximately one revolution. This wave becomes more distorted the closer the probe is to the wing, with the higher frequency oscillations becoming dominant. This is the greater influence of the blade tip vortex and wing-fuselage junction acoustics.

The wing probes (Figure 11(b)) show slightly lower values of noise on the wing in comparison to the fuselage. Only the influence of the front propellers is seen on the wing, thus losing the influence of the wing-fuselage pivot junction waves. The sound pressure levels oscillate between 0.9 and 0.6 with an average value of 0.83. Slightly higher averages are observed for the probes furtherest away from the fuselage either side of each nacelle, with the highest average of 0.86 seen at the wing tip.

The ground probes (Figure 11(c)) indicate sound pressure levels of between 0.5 and 0.7 three span lengths underneath

the aircraft. The influence of the front and rear propellers can be observed with the increased number of blades for the front propellers resulting in higher frequency content for the furtherest forward probe, with a lower frequency waves present at the rear. Very similar trends are observed for the two centre probes with the peaks seen earlier behind the wing.

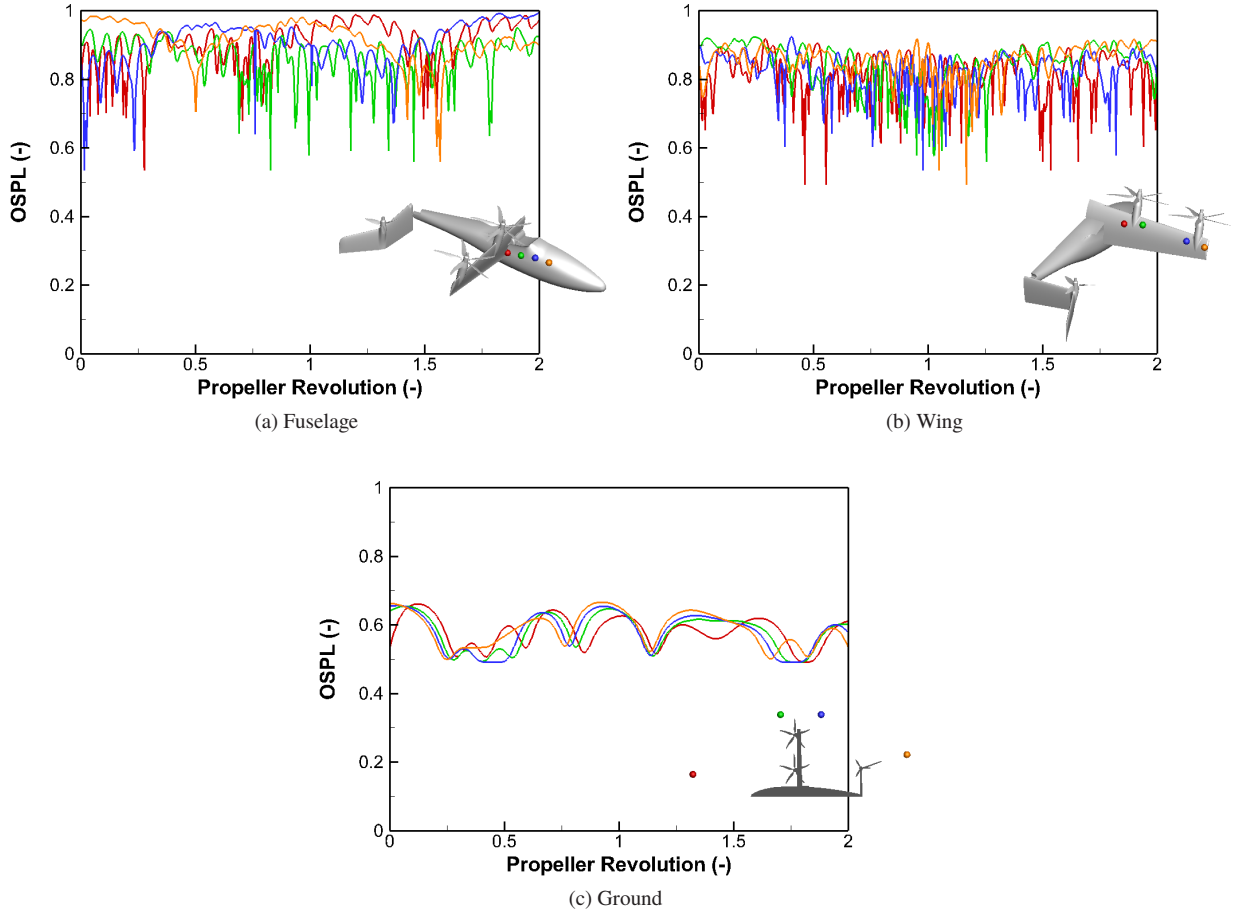

(a) Fuselage

(b) Wing

(c) Ground

Fig. 11 OSPL of the numerical probes for the aircraft in hover

Results of the Semi-Span Aircraft in Forward-Flight

Following on from the hover simulation, using the adjusted grid, the aircraft was simulated in forward-flight. Although the aim of the aircraft design is for vertical take-off/landing, the majority of the flight plan will be with the aircraft in forward-flight configuration.

Aerodynamics

Due to influence of the axial velocity, a stable aerodynamic solution is observed. The folding of the front propellers has allowed for a cleaner inflow to the rear with the freestream velocity projecting the blade tip vortices across the tail.

This can be seen in Figure 12 where the flow-field is visualised using slices with Q-criterion contours. Oscillations in loads are observed across the tail and rear propeller blades, with the impinging blade tip vortex resulting in oscillation in drag and lift for the tail. The propeller blade thrust coefficients fluctuate as each blade passes the tail with a greater reduction in loads observed as the blade crosses the horizontal section. The sweep angle of the vertical stabilser produces a reduction in blockage effect. With only the freestream conditions acting on the fuselage and wing, the drag and lifting forces reach a stable equilibrium for both components.

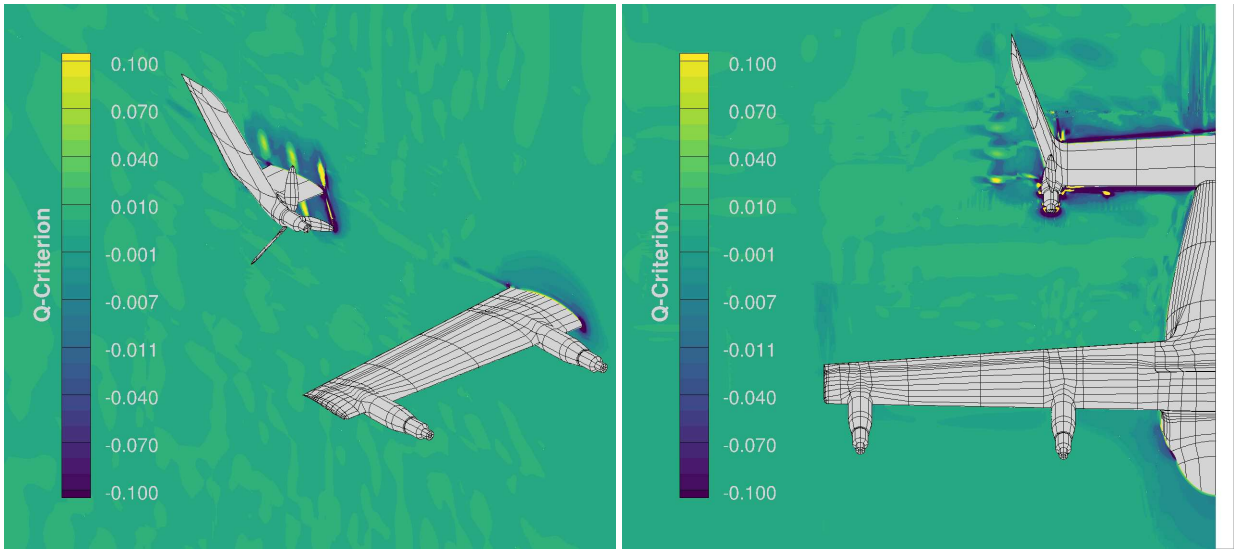

(a) Side slice (b) Vertical slice

Fig. 12 Flow visualisation around the rear propeller in forward-flight

Acoustics

Presented in Figure 13(a) is the aircraft surface overall sound pressure level for the forward-flight condition. The maximum OSPL has been kept constant to show the difference between hover and forward-flight. In comparison to the hover simulation, a significant decrease in the acoustic emissions is observed. Large pockets of sound waves below 0.8 are observed across the fuselage and wing, with all the higher value acoustics seen on the tail and propeller blades. On average, the hover flight condition results in an overall sound pressure level of 0.83. This reduces to 0.73 in forward flight, a 10% reduction. This 10% reduction is seen mainly across the fuselage and wing components with an 8% reduction seen on the tail.

Figure 13(b) presents the time-history of two fuselage probes. Focusing on the second revolution where the acoustic results have converged, the sound levels oscillate between 0.4 and 0.7. Despite the attached aerodynamic solution, the sound waves generated from the rear propeller propagate towards the front of the aircraft causing these oscillations. Some higher frequency content can be observed and this is a result of how the sound waves travel across the wing.

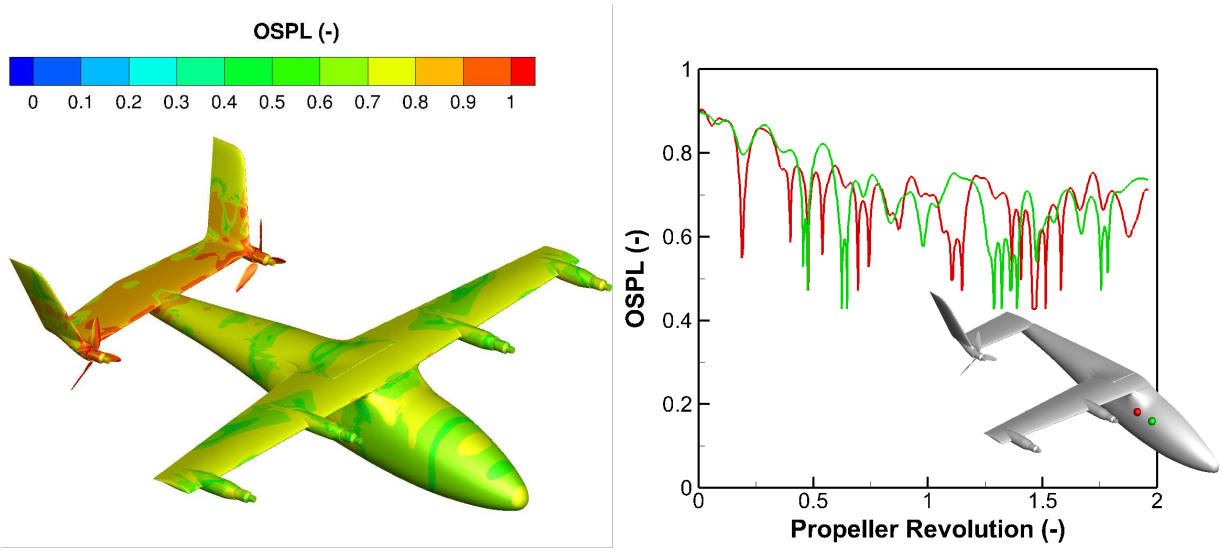

(a) Aircraft surface solution

(b) Fuselage probe time-history

Fig. 13 Aircraft OSPL in forward-flight

Synchrophasing Analysis

The technique of propeller synchrophasing is introduced to the eVTOL aircraft in order to mitigate the acoustics emissions. Synchrophasing involves the introduction of a phase shift between propellers. Figure 14 presents a schematic of the technique. For a twin-engine turboprop aircraft, significant benefits were found [22].

The proposed synchrophasing configuration for the eVTOL aircraft in forward-flight are presented in Figure 14. Due to the folding of the front propellers in forward flight, only the rear propeller blades have to be adjusted. Using the port propeller as the reference, the starboard propeller is shifted by 27.5° . This phase shift results in the starboard propeller being in-between the vertical and horizontal tail components as the port side is crossing the tail. The aim of this synchrophasing configuration is to ensure the periodic oscillation in blade loads only occurs in one blade at a given instance in time.

Due to the lack of symmetry in the propeller phase, synchrophased simulations required the full aircraft geometry. The same conditions as the semi-span aircraft is selected (Table 3).

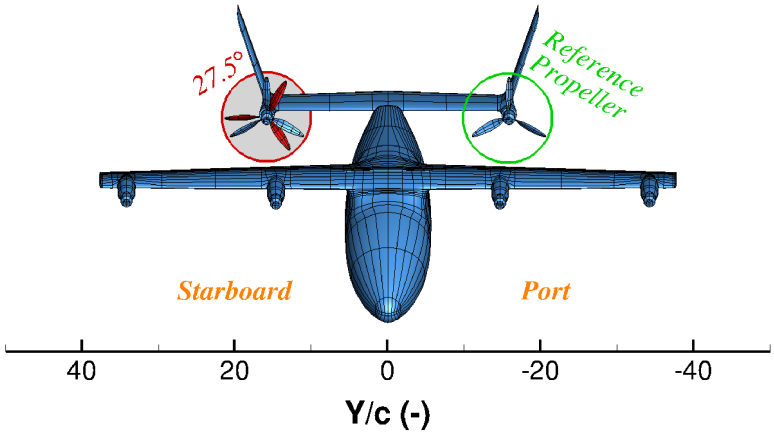

Fig. 14 Synchrophasing schematic

Results of the Synchrophased Aircraft in Forward Flight

Aerodynamic Results

Presented in Figure 15 is the individual blade and combined propeller normalised thrust coefficients for the starboard and port propellers with the same trend observed in the baseline configuration. The loads have been normalised with respect to the same average value as the baseline hover simulation. There is a drop in load as the blade passes each section of the tail, with a larger reduction seen as the blade passes the horizontal section. As a result of the introduction of the phase shift, the peak in full propeller load for the starboard rotor now occurs later. This is beneficial for the acoustic emissions as the port propeller peak is seen before and thus avoiding the maximum values occurring at the same instance.

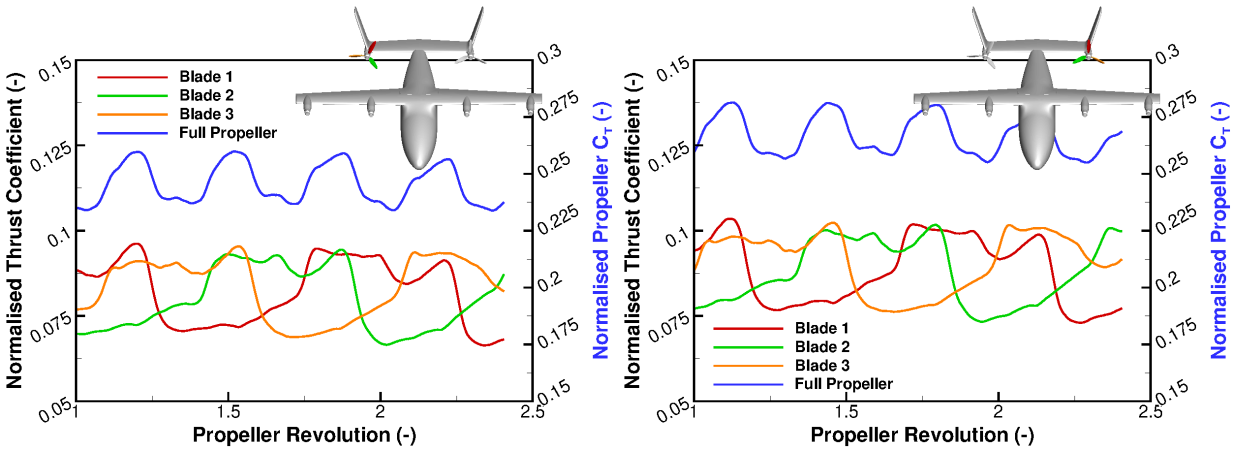

(a) Starboard propeller

(b) Port propeller

Fig. 15 Cruise propeller normalised C_T time-history

The aircraft normalised surface pressure coefficient is presented in Figure 16 with a comparison made to the baseline configuration. A very similar trend is captured between the two simulations. Two stagnation points are seen on the fuselage. The first at the aircraft nose and a second near the wing-fuselage junction. Almost the entire upper wing surface is suction pressure and this results in the largest force acting on the aircraft being the wing lift. The pressure profile across the tail fluctuates due to the influence of the propeller flow. This is seen on the outer side of the starboard vertical stabiliser. There is an additional loss of suction pressure at the centre of the tail. This is due to the slight overhang of the fuselage junction thus creating detached flow.

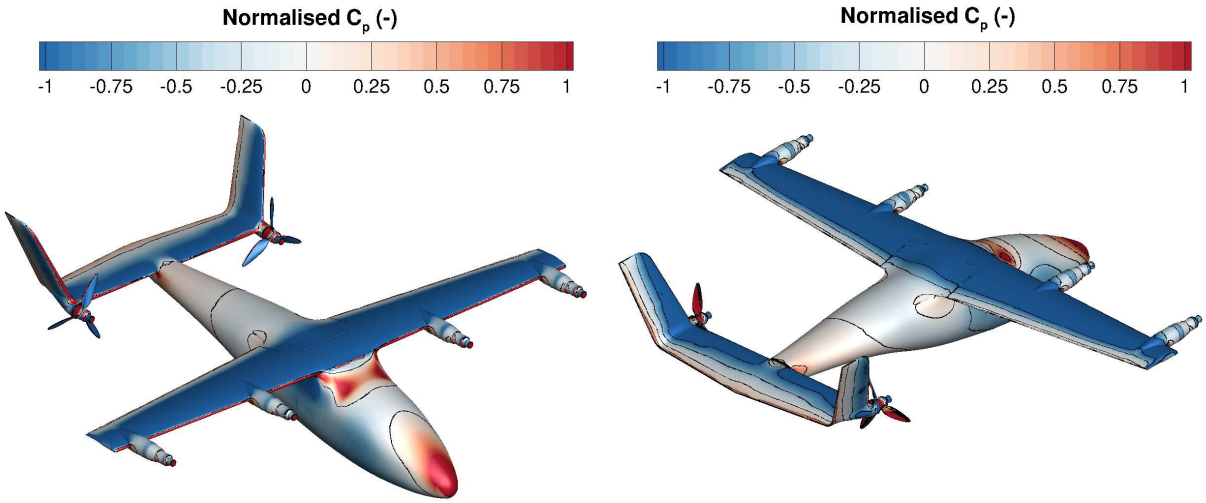

Fig. 16 Synchrophased aircraft normalised surface pressure coefficient in forward-flight

Presented in Figure 17 is the flow-field visualisation for the synchrophased aircraft using slices of Q-criterion. As expected, the same trend as the baseline configuration (Figure 12) is captured. The blade tip vortices are captured across both sides of the aircraft.

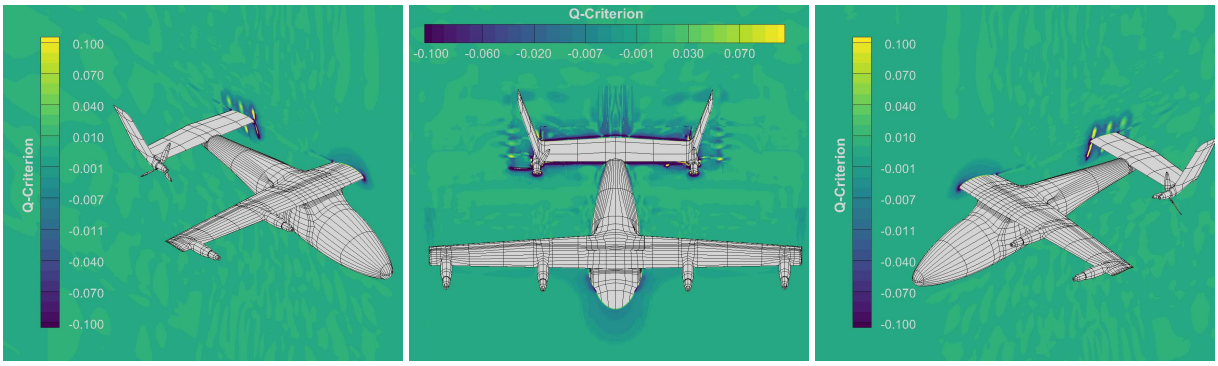

Fig. 17 Synchrophased aircraft flow-field visualisation using slices with Q-criterion

Acoustic Results

Presented in Figure 18 is the difference in overall sound pressure level between the synchrophased and baseline configurations for two flow-field slices. Differences of 20% of the maximum OSPL value are observed with the greatest differences found on the starboard side. On the axial slice (Figure 18(a)), a reduction in acoustics is seen between the two propellers. This is a result of the interaction of sound waves between the two propellers balancing. The sound waves propagated outwards of the starboard wing tip are pushed further outboards from the aircraft with a band of reduced OSPL seen around the wing tip. This is seen on both the axial and horizontal slices.

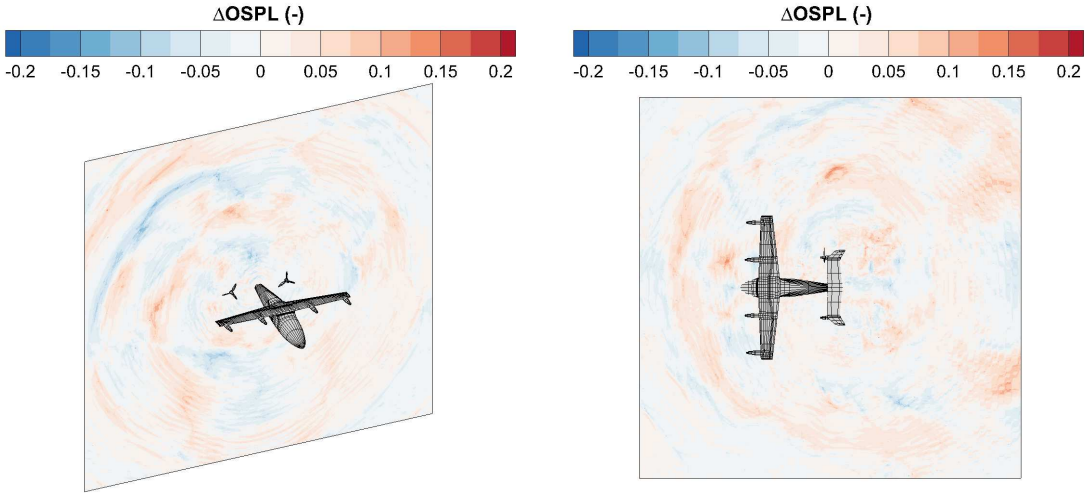

(a) Axial slice (b) Horizontal slice

Fig. 18 Difference in OSPL between the synchrophased and baseline configurations for the axial and horizontal slices

Presented in Figure 19 is the averaged surface overall sound pressure level for both the baseline and synchrophased configurations. As observed, values between 0.9 and 0.5 are seen across the aircraft surface. For the baseline configuration an average value of 0.7012 is seen with a reduction to 0.6985 with the introduction of the synchrophasing. The high values of noise are seen around the tail and propeller blade, as expected. Looking at the horizontal section of the tail, on the port side the trends between the synchrophasing and baseline configurations are similar. The majority of the upper surface has values above 0.75 with pockets above 0.8 towards the leading edge. On the starboard side, difference are observed. A pocket of lower value acoustics is seen between the propeller and centre section of the tail. This helps reduce the overall sound pressure level across the aircraft as the peaks and troughs of the port/starboard propeller waves balance resulting in the reduction.

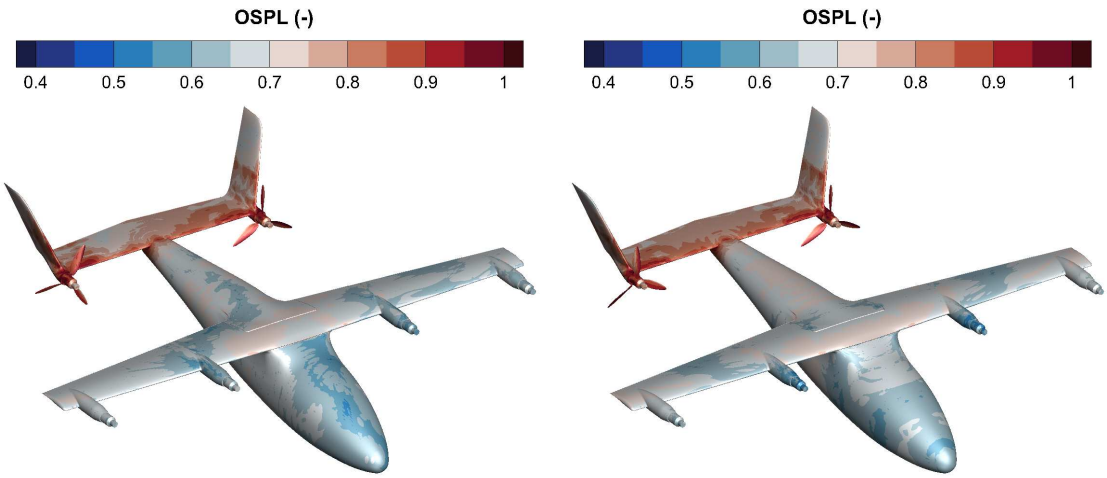

(a) Synchrophased (b) Baseline

Fig. 19 Comparison of the averaged surface OSPL between the synchrophased and baseline configurations

Presented in Figure 20 is the comparison of the surface averaged non-dimensional OSPL between the synchrophased and baseline configurations at the fuselage cabin. In terms of average values and mirroring the full aircraft surface, a slightly lower value of OSPL is seen with the synchrophased configuration as a value of 0.636 is derived. This compares to the average baseline value of 0.645. Around the fuselage azimuth, the difference in OSPL oscillates between the two configurations. At the starboard and port sides (0° and 180° , respectively), a slight increase in OSPL is seen for the synchrophasing. This equates to a maximum difference of 0.052 and 0.035 on the port and starboard sides, respectively. The opposite is found around the top and starboard lower section. Here, reductions of 0.076 and 0.068 are seen, respectively.

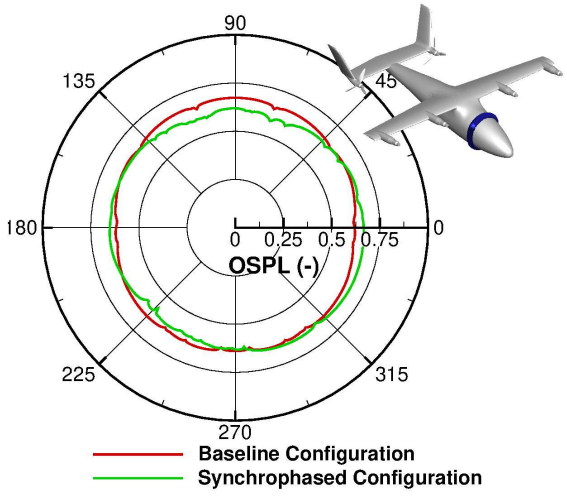

Fig. 20 Comparison of the average non-dimensional surface OSPL between the synchrophased and baseline configurations at the fuselage cabin

Conclusions

Baseline and Synchrophasing Conclusions

The following conclusions are observed from the baseline configuration simulations in hover and forward flight:

- It is clear from the baseline configurations that the hover flight condition is more critical in terms of the acoustics levels compared to forward flight. The use of the front propellers for vertical take-off significantly amplifies the noise levels around the fuselage cabin with acoustic levels above 0.7. Not only are higher levels of acoustics seen on the aircraft surface, the flow-field slices indicate a propagation of noise further outwards of the vehicle.
- In forward flight, the acoustics emissions are significantly reduced with the majority of high level noise contained around the aircraft tail.
- The introduction of synchrophasing to the aircraft in forward-flight found an altering in sound pattern and thus seeing a reduction in sounds level across the aircraft surface, with the numerical probe and flow-field data indicating the shifting in pattern across the starboard side.
- One of the critical observations from the investigation is the significant oscillations in sounds waves around the fuselage-tail junction. In both hover and forward-flight, the high frequency waves propagate into the flow-field and interact with the tonal noise generated from the propellers. Such oscillations not only indicate an additional source of noise but also a potential vibration source.

Acknowledgments

The authors would like to thank Roll-Royce for their support and permission to publish the work. This work used the Cirrus UK National Tier-2 HPC Service at EPCC (`https://www.epcc.ed.ac.uk/cirrus`) funded by the University of Edinburgh and EPSRC (EP/P020267/1) under project number EC004. Results were obtained using the ARCHIE-WeSt High Performance Computer (`http://www.archie-west.ac.uk/`) based at the University of Strathclyde.

References

[1] Ng, W., and Datta, A., "Hydrogen Fuel Cells and Batteries for Electric-Vertical Takeoff and Landing Aircraft," *Journal of Aircraft*, Vol. 56, No. 5, 2019. DOI: 10.2514/1.C035218.

[2] Whittle, R., "The Demand for On-Demand Mobility," *Vertiflite*, 2017, pp. 34–38. January/February.

[3] Arguelles, P., Bischoff, M., Busquin, P., Droste, B., Evans, S. R., Kroll, W., Lagardere, J., Lina, A., Lumsden, J., Ranque, D., Rasmussen, S., Reutlinger, P., Robins, S. R., Terho, H., and Wittlov, A., "EUROPEAN AERONAUTICS: A VISION FOR 2020: Meeting society's needs and winning global leadership," Tech. rep., European Commission, 2001.

[4] Darecki, T. M., Edelstenne, C., Enders, T., Fernandez, E., Herteman, P. H. J., Kerkloh, M., King, I., Ky, P., Mathieu, M., Orsi,

G., Schotman, G., Smith, C., and Worner, J., "Flightpath 2050: Europes vision for aviation. report ofthe high level group on aviation research," Tech. rep., ACARE (Advisory Councilfor Aeronautics Research in Europe), 2011.

[5] Dehaeze, F., and Barakos, G., "Mesh deformation method for rotor flows," *Journal of Aircraft*, Vol. 49, No. 1, 2012, pp. 82–92. DOI: 10.2514/1.C031251.

[6] Chirico, G., Barakos, G., and Bown, N., "Numerical aeroacoustic analysis of propeller designs," *The Aeronautical Journal*, Vol. 122, No. 1248, 2018, pp. 283–315. DOI: 10.1017/aer.2017.123.

[7] Crozon, C., Steijl, R., and Barakos, G., "Coupled flight dynamics and CFD - demonstration for helicopters in shipborne environment," *The Aeronautical Journal*, Vol. 122, No. 1247, 2018, pp. 42–82. DOI: 10.1017/aer.2017.112.

[8] Babu, S., Loupy, G., Dehaeze, F., Barakos, G., and Taylor, N., "Aeroelastic simulations of stores in weapon bays using Detached-Eddy Simulation," *Journal of Fluids and Structures*, Vol. 66, 2016, pp. 207–228. DOI: 10.1016/j.jfluidstructs.2016.07.014.

[9] Scrase, N., and Maina, M., "The Evaluation of Propeller Aero-acoustic Design Methods by Means of Scaled-Model Testing Employing Pressure Tapped Blades and Spinner," *19th ICAS Congress, Anaheim, California, USA.*, International Council of the Aeronautical Sciences, 1994. ISBN: 1563470845.

[10] Gomariz-Sancha, A., Maina, M., and Peace, A., "Analysis of propeller-airframe interaction effects through a combined numerical simulation and wind-tunnel testing approach," *53rd AIAA Aerospace Sciences Meeting*, AIAA, Kissimmee, Florida, 2015. DOI: 10.2514/6.2015-1026.

[11] Knepper, A., and Bown, N., "IMPACTA Wind-tunnel Instrumentation Specification," Tech. Rep. ITS 01777, Issue 3, Dowty Propellers (GE Aviation Systems Ltd), 2014.

[12] Barakos, G., and Johnson, C., "Acoustic comparison of propellers," *International Journal of Aeroacoustics*, Vol. 15, No. 6-7, 2016, pp. 575–594. DOI: 10.1177/1475472X16659214.

[13] Higgins, R., Jimenez-Garcia, A., Barakos, G., and Bown, N., "High-Fidelity Computational Fluid Dynamics Methods for the Simulation of Propeller Stall Flutter," *AIAA Journal*, Vol. 57, No. 12, 2019. DOI: 10.2514/1.J058463.

[14] Higgins, R., Barakos, G., and Jinks, E., "Estimation of Three-Dimensional Aerodynamic Damping using CFD," *The Aeronautical Journal*, Vol. 124, No. 1271, 2019. DOI: 10.1017/aer.2019.135.

[15] Higgins, R., Zarev, A., Barakos, G., and Green, R., "Numerical Investigation of a Two-Bladed Propeller Inflow at Yaw," *Journal of Aircraft*, Vol. 57, No. 2, 2020. DOI: 10.2514/1.C035647.

[16] Garcia, A. J., Barakos, G., and Gates, S., "Tiltrotor CFD Part I - validation," *The Aeronautical Journal*, Vol. 121, No. 1239, 2017. DOI: 10.1017/aer.2017.17.

[17] Jarkowski, M., Woodgate, M., Barakos, G., and Rokicki, J., "Towards Consistent Hybrid Overset Mesh Methods for Rotorcraft CFD," *International Journal for Numerical Methods in Fluids*, Vol. 74, No. 8, 2014, pp. 543–576. Doi:10.1002/fld.3861.

[18] Spalart, P., "Detached-Eddy Simulation," *Annual Review of Fluid Mechanics*, Vol. 41, 2009. DOI: 10.1146/annurev.fluid.010908.165130.

[19] Spalart, P., Deck, S., Shur, M., Squires, K., Strelets, M., and Travin, A., "A New Version of Detached-Eddy Simulation, Resistant to Ambiguous Grid Densities," *Theoretical and Computational Fluid Dynamics*, Vol. 20, 2006. DOI: 10.1007/s00162-006-0015-0.

[20] Menter, F., and Egorov, Y., "The Scale-Adaptive Simulation Method for Unsteady Turbulent Flow Predictions. Part 1: Theory and Model Description," *Flow, Turbulence and Combustion*, Vol. 85, No. 1, 2010. DOI: 10.1007/s10494-010-9264-5.

[21] Menter, F., and Egorov, Y., "A Scale Adaptive Simulation Model using Two-Equation Models." *43rd AIAA Aerospace Sciences Meeting and Exhibit*, 2005. DOI: 10.2514/6.2005-1095.

[22] Chirico, G., Barakos, G., and Bown, N., "Propeller installation effects on turboprop aircraft acoustics," *Journal of Sound and Vibration*, Vol. 424, 2018. DOI: 10.1016/j.jsv.2018.03.003.